Supporting Information

A mechanistic approach to evaluating atmospheric deposition of micro- and nanoplastic particles

Marianne Seijo[a], Michael J. Whelan[b], Todd Gouin[c], Antonia Praetorius*[, a]

[a] Institute for Biodiversity and Ecosystem Dynamics (IBED), University of Amsterdam, The Netherlands
[b] School of Geography, Geology and the Environment, University of Leicester, UK
[c] TG Environmental Research, Sharnbrook, Bedfordshire, United Kingdom

*Corresponding author:
Antonia Praetorius
a.praetorius@uva.nl
Tel. +31 20 525 1279

Table of Contents

Section S1: Abbreviations

Table S1: List of abbreviations (units)

A	Characteristic radius of collectors depending on land-use categories (m)
C	Atmospheric concentration of MNPs (μg m^{-3})
C_c	Cunningham correction factor (-)
C_D	Drag coefficient (-)
c_p	Heat capacity of air ($m^2.s^{-2}.K^{-1}$)
D_p	Raindrop diameter (m)
D_{diff_Br}	Particle Brownian diffusivity ($m^2.s^{-1}$)
D_{diff_Water}	Water vapour diffusivity in air ($m^2.s^{-1}$)
DLA	Diffusion Limited Aggregation
d_f	Fractal dimension (-)
d_p	Particle diameter (m)
$E\ (d_p, D_p)$	Overall collection efficiency (-)
$E_{th}\ (d_p, D_p)$	Collection efficiency due to thermophoresis (-)
$E_{dph}\ (d_p, D_p)$	Collection efficiency due to Diffusiophoresis (-)
$E_{ec}\ (d_p, D_p)$	Collection efficiency due to charge effect (-)
e	Elongation of the fiber (-)
F_N	Newton form factor (-)
F_S	Stokes form factor (-)
f	Flatness of the fiber (-)
g	Acceleration of gravity ($m.s^{-2}$)
I	Intermediate dimension of the fiber (m)
k_a	Thermal conductivity of air ($J.m^{-1}.s^{-1}.K^{-1}$)
k_p	Thermal conductivity of the MNP ($J.m^{-1}.s^{-1}.K^{-1}$)
$k_{N,\ A}$	Newton drag correction for average orientation (-)
$k_{N,\ rand}$	Newton drag correction for random orientation (-)
$k_{N,\ hor}$	Newton drag correction for horizontal orientation (-)
$k_{S,\ A}$	Stokes drag correction for average orientation (-)
$k_{S,\ rand}$	Stokes drag correction for random orientation (-)
$k_{S,\ hor}$	Stokes drag correction for horizontal orientation (-)
k_x	Structure prefactor (also called lacunarity or structure factor). *Here x denotes hydrodynamical radius or radius of gyration (m)*
L	Longest dimension of the fiber (m)

L_{MO}	Monin–Obukhov length (m)
M_a	Molecular weight of air ($g.mol^{-1}$)
M_w	Molecular weight of water ($g.mol^{-1}$)
N	Number of particles in an aggregate (-)
$N(Dp)$	Raindrop size distribution (-)
P	Atmospheric pressure (Pa)
P_a^0	Water vapor pressure at temperatures T_a, ($g.cm^{-1}.s^{-2}$)
P_S^0	Water vapor pressure at temperatures T_S, ($g.cm^{-1}.s^{-2}$)
Po	Porosity of an aggregate (-)
Q_r	Mean charges on the raindrop (C)
q_p	Mean charges on the particle (C)
R	Universal gas constant (= 8.3144598 $J{\cdot}K^{-1}{\cdot}mol^{-1}$)
R_A	Aerodynamic resistance ($m.s^{-1}$)
Re	Reynolds number (-)
Re_r	Raindrop Reynolds number (-)
RH	Relative humidity (-)
RLA	Reaction Limited Aggregation
R_i	Fraction of particles stuck to a surface (-)
RI	Rain Intensity ($mm.h^{-1}$)
R_S	Surface resistance ($m.s^{-1}$)
R_x	Radius of aggregate. Here x denotes hydrodynamical radius or radius of gyration (m)
r_c	Radius of the larger cluster forming the aggregate (m)
r_p	Radius of the particle (m)
S	Small dimension of the fiber (m)
Sc	Schmidt number (-)
Sc_w	Schmidt number for water vapor in air (-)
S_t	Stokes number (-)
T_a	Air temperature (K)
T_S	Temperature of the raindrop surface(K)
u_*	Friction velocity ($m.s^{-1}$)
$V(Dp)$	Raindrop terminal velocity ($m.s^{-1}$)
V_0	Volume of a particle in a monodispersed aggregate (m^3)
V_A	Volume of an aggregate (m^3)
V_i	Volume of a particle *i* in a polydispersed aggregate (m^3)

v_d	Dry deposition velocity ($m.s^{-1}$)
v_g	Dry settling velocity in Newton regime, also called gravitational velocity ($m.s^{-1}$)
v_p	Dry settling velocity of a permeable aggregate ($m.s^{-1}$)
v_s (v_g)	Dry settling velocity in Stokes and Brownian regime ($m.s^{-1}$)
z_0	Roughness length from the land (m)
z_R	Height of the canopy (m)
χ	Shape factor (-)
Γ	Ratio of the settling velocity of a permeable (v_p) on impermeable aggregate (v_g) (-)
Ψ_H	Stability function (-)
κ	von Karman constant (-)
κ_p	Floc permeability (m^2)
λ_p	Scavenging coefficient (s^{-1})
μ	Fluid viscosity (Pa.s)
μ_a	Air viscosity (Pa.s)
μ_w	Water viscosity (Pa.s)
ν_A	Kinematic viscosity of the water ($m^2.s^{-1}$)
ρ	Fluid density ($kg.m^{-3}$)
ρ'	Density ratio (-)
ρ_a	Air density ($kg.m^{-3}$)
ρ_p	Particle density ($kg.m^{-3}$)
σ_w	Water surface tension ($N.m^{-1}$)
λ	Mean free path of the fluid (m)
ζ	Dimensionless permeability of the porous aggregate (-)

37

38

Section S2: Dry deposition

Overview of the different processes contributing to the dry deposition of particles form the atmosphere (Figure S1). Dry deposition is a combination of dry settling and resistance deposition near surfaces. Dry settling occurs as particles move downward in the air column under the influence of gravitational, buoyancy, and drag forces and, depending on particle size, is best described by Brownian, Stokes or Newton processes. Resistance deposition takes place when particles approach and interact with obstacles close to the surface during the deposition process, as well as the aerodynamic conditions near this surface. It is influenced by the surface characteristics, the intensity of surface winds and the particle size.

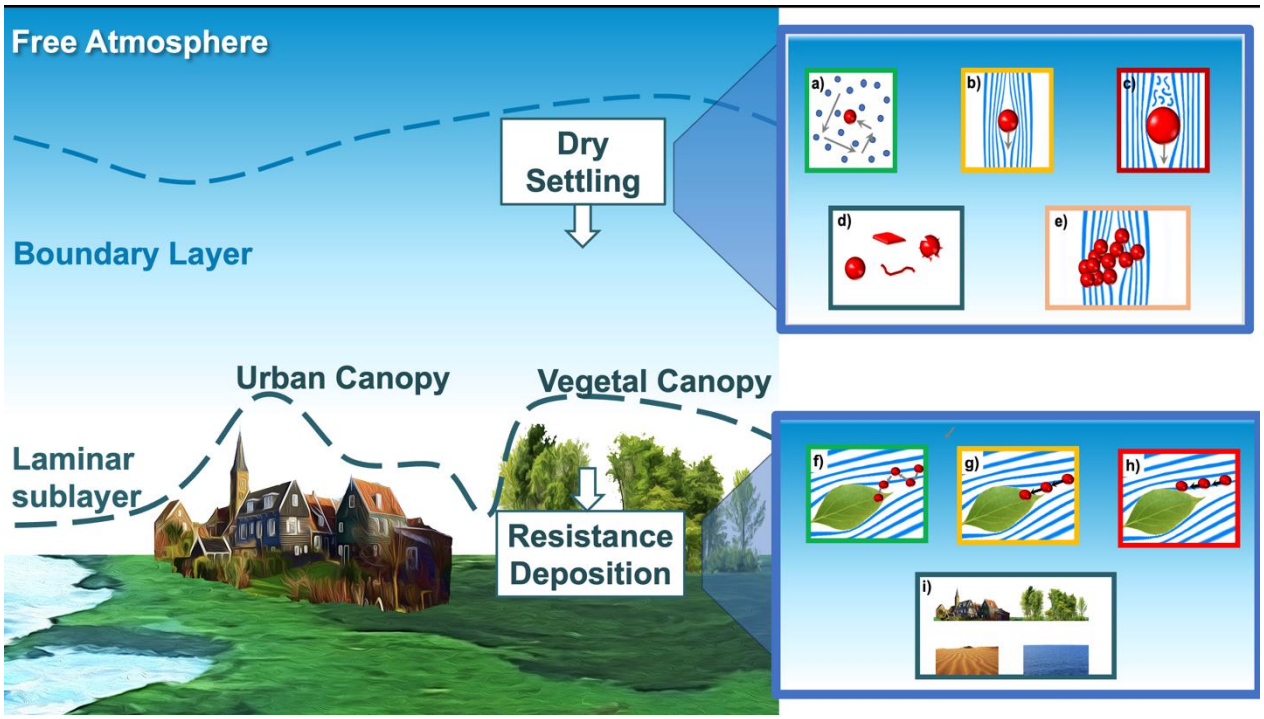

Figure S1 Dry Deposition The dry deposition of particles is the sum of dry settling in the well-mixed boundary layer and resistance deposition in the laminar sublayer. Dry settling depends on particle size: from a) Brownian regime, to b) Stokes regime, to c) Newton regime, but also d) the shape of the particle and e) the porosity and permeability of particle aggregates. Resistance deposition depends on the collision efficiency between the particle in laminar flow and the deposition surface, via f) Brownian diffusion, g) Inertial impaction, h) Interception, i) and the local surface's height, nature, and smoothness. (Figure illustration created by the authors with Adobe Suite, partially inspired by Framer et al. illustrations[1]).

Section S2.1:Dry settling velocity

Spherical MNPs in Newton regime (d_p > 75.75 µm)

In Newton's regime, the terminal velocity (v_g) for dry settling of spherical particles is calculated from the particle diameter (d_p), the fluid density (here: air) (ρ), the drag coefficient C_D, the gravitational constant (g) and the particle density (ρ_p), as [2]:

$$v_g = \sqrt{\frac{4 d_p g (\rho_p - \rho)}{3 C_D \rho}} \qquad \text{Eq. S1}$$

C_D is a unitless number that depends on particle shape, flow distribution, orientation, permeability. Type of flows are defined by Reynolds number. There is the Laminar flow with Re lower than unity, and turbulent flow, characterized by a high Reynolds number. A transitional regime exists between laminar and turbulent regimes, in which a correlation is needed to calculate C_D. In this transitional regime, numerous spherical drag correlations have been presented in the literature. Based on recent benchmark experimental data of spherical particles,[3] it has been determined that the correlation proposed by Kalman and Matana[4], presented in Table S2, is the most appropriate fit for the transitional regime, but also the entire range of Re, as it is the one with the lowest average relative error. Therefore, this correlation is used as the standard spherical drag coefficient in this study.

Table S2: Drag coefficient equations used in this work, for impermeable spherical particles in different types of flow (defined by Reynolds number Re). Based on Kalman and Matana[4]

Type of flow	Reynolds Number, Re	Drag coefficient, C_D
Laminar	Re < 1	$C_D = \frac{24}{Re}$
Transitional	1 < Re < 1000	$C_D = \frac{24}{Re} + \frac{5}{Re^{0.6}} + 0.44$
Turbulent	1000 < Re < $2x10^5$	~ 0.44
Turbulent	$2x10^5$ < Re	0.10

Spherical MNPs in Stokes regime (16.7 µm < d_p ≤ 75.75 µm)

In Stokes' regime, the strength of viscous forces at the surface of the particle is a key force. According to Stokes' law, the terminal velocity (v_g) for dry settling of particles is here calculated from the particle diameter (d_p), the fluid density—here the air—(ρ), the fluid viscosity (μ), the gravitational constant (g) and the particle density (ρ_p) as follows:

$$v_g = \frac{g}{18\mu} (\rho_p - \rho) {d_p}^2 \qquad \text{Eq. S2}$$

Stokes' law (Eq. S2) is limited to spherical, smooth, and rigid particles in laminar flow (Re < 1, d_p < 50 μm), with no interactions with other particles (dilute suspensions), and uniform density, in a continuous fluid medium. Equations for other conditions beyond these constraints will be presented later.

Spherical MNPs in Brownian regime ($d_p \leq 16.7$ µm)

The derivation of Stokes' law assumes a no-slip condition which is no longer correct for very small particles. When particles are small enough to be at or below the same size as the mean free path of the fluid (the distance a fluid molecule travels before colliding with neighboring fluid molecules), this fluid can no longer be considered as a continuous medium. The mean free path on dry air is 66 nm at 23 °C, 1 atm.[5]

On this Brownian scale, the Cunningham correction factor,[6] C_c, applied allows for predicting the terminal velocity of small particles v_s in a fluid:

$$v_s = v_g C_c \qquad \text{Eq. S3}$$

Where the Cunningham correction factor, C_c, is defined as

$$C_C = 1 + \frac{2\lambda}{d_p}\left(A_1 + A_2 exp\left(\frac{-A_3 d_p}{2\lambda}\right)\right) \qquad \text{Eq. S4}$$

Where λ is the mean free path of the fluid molecules, A_n are experimentally determined coefficients. Here we use the coefficients presented by S. G. Jenning[7] for air: A_1 = 1. 252, A_2 = 0 .399, A_3 = 1.100, λ = 6.635x10^{-8} m.

The limit between Stokes and Newtonian regimes for the dry settling of MNPs

The size threshold separating the Stokes and Newtonian regimes can be calculated from the particle Reynolds number, Re_p. This indicates if the flow regime around the particle is laminar (when $Re_p \leq 1$ in the air, Stokes regime) or turbulent (when $Re_p > 1$ in the air, Newtonian regime). Re_p is defined as:

$$Re_p = \frac{\rho_a v_g d_p}{\mu_a} \qquad \text{Eq. S5}$$

where ρ_a is the density of air (kg m^{-3}), v_g is the terminal dry settling velocity of the particle (m s^{-1}), d_p is the particle diameter (m), and μ_a is the dynamic viscosity of air (kg^{-1} s^{-1}).

In Figure S2 a), the critical mean diameter of MNPs (with a density range between 900 and 1600 kg m^{-3}), above which dry settling follows the Newtonian region, is determined to be 75.73 µm. For comparison, for mineral dust particles, due to their higher density (2000–5000 kg m^{-3}), this mean diameter is calculated to be 52.09 µm. In contrast, for pollens with densities similar to or lower than MNPs (600-1200 kg m^{-3}), this

value is found to be 85.18 µm. Further details on the low and high densities applied for each material are provided in the caption of Figure S2. Note that when extending the density range of MNPs to include very high-density polymers such as polytetrafluoroethylene (PTFE), the mean cut-off diameter between Newton and Stokes is lowered to around 72 µm.

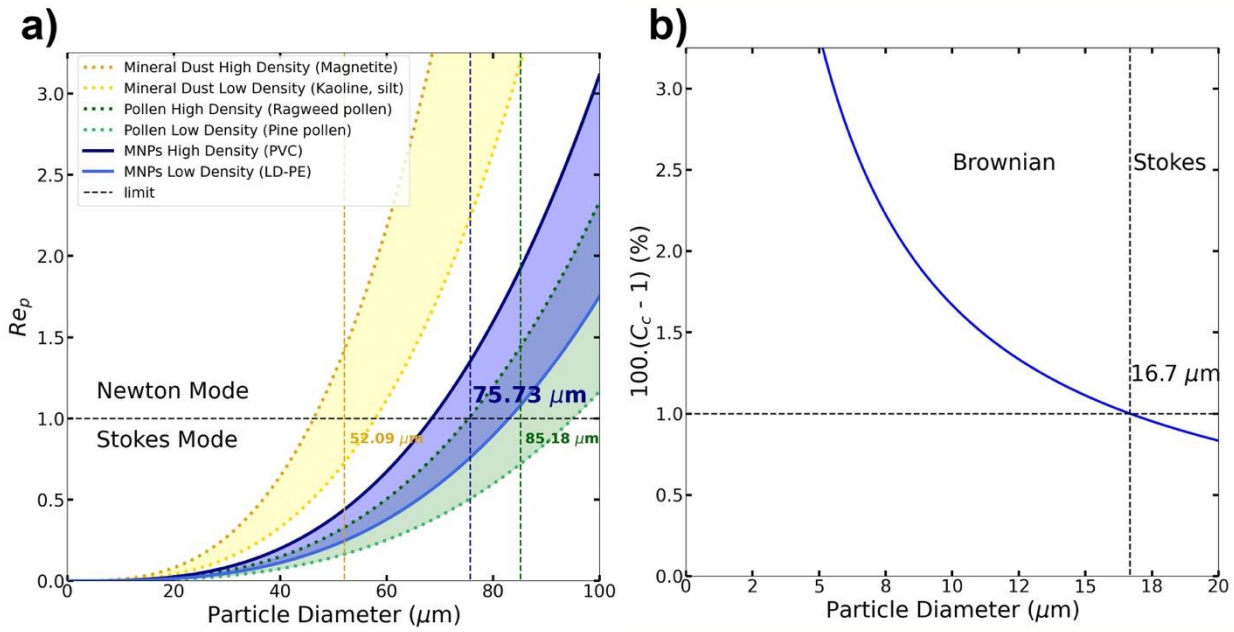

Figure S2: MNPs Dry Settling in air: Brownian, Stokes and Newtonian modes boundary limits. a) Limit between Newtonian and Stokes modes. This figure shows how the particle Reynolds number (Rep) varies with particle diameter for MNPs, mineral dust, and pollen, across different density ranges. The Rep = 1.0 line marks the threshold between Newtonian and Stokes regimes. The blue shaded area represents MNPs densities (900–1600 kg/m³ corresponding to LD-PE and PVC respectively) with a transition diameter at 75.73 µm. For comparison, mineral dust (yellow, 2000–5000 kg/m³, kaolinite and magnetite respectively) transitions at 52.09 µm, and pollen (green, 600–1200 kg/m³, pine pollen and Ragweed pollen respectively) at 85.18 µm.**b) Limit between Brownian and Stokes modes.** Variation of the Cunningham correction (C_c) as a function of particle diameters. The Cunningham correction is required for particles < 16.7 μm to keep the error below 1%, delimited in this work the Brownian and Stokes regimes.

Unlike the Newton-Stokes limit, the limit between the Stokes and Brownian regimes is dependent mostly on particle size. For particle sizes near to or below the mean free path of fluid molecules, the Stokes regime's aerodynamic theory is no longer appropriate to describe particle motion through the fluid. Based on Eq. S4, Figure S2 b) shows Cunningham correction factor (expressed as a percentage) for different particle sizes below 20 µm. To limit the error in the evaluation of the settling velocity of small particles to 1%, the Cunningham correction should be applied to particles with a diameter of 16.7 μm or smaller. These values are recommended as average values for MNPs, and the authors encourage calculating specific values for each type of particle.

Impact of particle density on dry settling velocity

The influence of MNP size and density on the dry settling of MNPs is illustrated in Figure S3a for PVC (density: 1580 kg m^{-3}), PA as Nylon (density: 1130 kg m^{-3}), High-Density PE (density: 980 kg m^{-3}), and Low-Density PE (density: 920 kg m^{-3}), each with sizes ranging from 0.1 to 1000 µm. The suspension of particles in the air is predicted to decrease rapidly as size and density increase due to gravitational effects. As can be seen in Figure S3**,** the impact or particle size is more pronounced than that of particle density for size and density ranges relevant for MNPs.

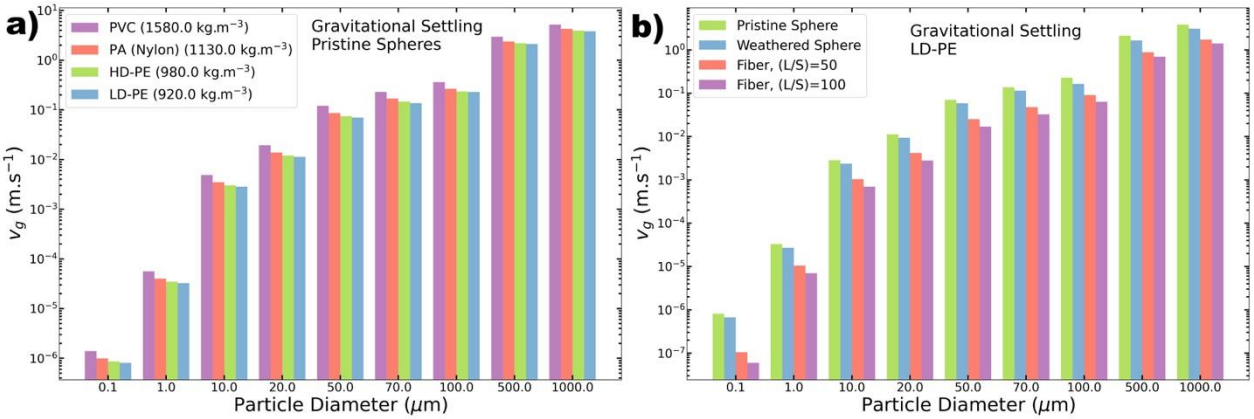

Figure S3: Effect of MNPs size, densities, and shapes on the gravitational settling. a) Densities and particle size effects on the gravitational settling: Gravitational settling velocities of PVC, PA, High-Density PE (HD-PE), and Low-Density PE (LD-PE) particles with smooth (pristine) spherical shapes as the function of the particle diameter. Are represented: Brownian size range, (with particles diameters d_p = 10 µm, 1.0 µm, and 0.1 µm); Stokes size range (d_p = 70 µm, 50.0 µm, and 20 µm); and Newton size range (d_p =1000 µm, 500.0 µm, and 100 µm)**; b) Particles Shapes effects on the gravitational settling.** Gravitational settling velocities of low-density PE, with different shapes: pristine sphere shape, weathered sphere shape (with a Stokes shape factor c=1.2). Fiber shape, with the distinction between the aspect ratio of 50 and 100 (aspect ratio defined as the ratio of the longest dimension (L) on the smallest dimension (S)). The Brownian, Stokes and Newtonian regimes are represented similarly as a).

Non-spherical MNPs: shape effects

Particle shapes give rise to different drag forces and terminal dry settling velocities, which would, in turn, affect the aerodynamic behaviour of the particles.[8] Over the years, shape factors have evolved to establish a connection between non-spherical properties and spherical characteristics.

For Newton's regime, the dry settling velocity becomes:[2]

$$v_g = \sqrt{\frac{4 d_p g (\rho_p - \rho)}{3 C_D \chi \rho}} \qquad \text{Eq. S6}$$

153 And for Stokes' regime (with C_c=1.0) and Brownian regime:

$$v_s = \frac{v_g C_c}{\chi} \qquad \text{Eq. S7}$$

154 This factor can be measured experimentally.[9] We present in Table S3 χ values found in the literature.

155 *Table S3: Shape factors (for Stokes and Newton equations) for common particle shapes (based on Wilson and Huang 1979,[10]*
156 *Crowder et al. 2002,[11] Hassan and Lau 2009[12]).*

Shape	Shape factor χ
Sphere	1.00
Rough surface (e.g. weathered)	1.20
Plate	1.50
Cube	1.08
Straight chain	1.10

157

158 ## Impact of weathering on dry settling velocity—the golf-ball effect

159 Pristine MNPs typically feature a smooth surface. However, with time, various factors, such as exposure to
160 cold temperatures, photoaging, abrasion, molecular aggregations on the surface, and environmental
161 conditions[13], lead to the development of surface roughness. Where we assess the influence of weathering on
162 the airborne transport of MNPs (Figure S3 b). Taking pristine spherical particles made of low-density
163 polyethylene (LD-PE) as an example, three distinct size regimes are assessed: Newtonian, characterized by
164 diameters of 1 mm, 0.5 mm and 0.1 mm; Stokes (70 μm, 50 μm and 20 μm); and Brownian (10 μm, 1.0 μm,
165 and 0.1 μm). We evaluate the impact of weathering on spherical plastic particles by increasing their surface
166 roughness until it reaches a level equivalent to a "pollen shape" (shape factor χ =1.2, see Table S3).

167 As depicted in Figure S3 b, under dry settling conditions, we observe that weathered particles exhibit a
168 smaller gravitational settling velocity when compared to their pristine, smooth counterparts, for each
169 diameter considered. The increased surface roughness of the particles results in greater turbulence at their
170 surface, which, in turn, heightens friction with the surrounding air, causing a reduction in the particle settling
171 velocity. This phenomenon is also referred to as the 'golf ball effect,' where aerodynamic design prolongs a
172 particle's time aloft and retards its descent, akin to how a golf ball's dimples allow it to linger in the air
173 longer than a smooth ball of comparable size and weight, by minimising air resistance.

174 **Fibers** have particular airborne characteristics due to their complex geometry[11]. Fibers are flexible, varying
175 in flatness and elongation, and can adopt multiple orientations (e.g., straight, semicircular) during settling.
176 This flexibility affects Reynolds numbers (Re) and drag coefficients (C_D), making fixed-shape models

inadequate. Bagheri and Bonadonna[14] developed models for flexible fibers across a wide Re range (up to 3×10^5), considering random, horizontal, and average orientations. According to recent investigations[15–17], experimentally controlled fibres settling measurements are compared successfully using the average method proposed by Bagheri and Bonadonna[14], definitions and chain of equations presented in **Error! Reference s ource not found.**.

In Figure S3 b, the dry settling velocity of LD-PE fibres is compared to that of pristine LD-PE spheres with the same equivalent volume (i.e. the same mass). We present calculations for two example aspect ratios (length/diameter): 50 and 100, representing different length-to-diameter combinations. For a given mass, fibrous shape has a lower gravitational velocity compared to a smooth or a rugous MNPs sphere. Longer fibres experience even lower velocities than shorter fibres. This phenomenon, explained by the buoyancy and surface area differences between these two shapes, is one of the important elements explaining the observed long-range transport of fibres in the atmosphere.[18]

Table S4: Definitions and chain of equations to calculate C_D (the drag coefficient of fibres) based on the method developed by Bagheri and Bonadonna,[14] from the calculation of the random and horizontal orientation drag corrections.

<table>
<tr><td colspan="6">Dimension of the fibre (m):</td></tr>
<tr><td colspan="2">Longest: L</td><td colspan="2">Intermediate: I</td><td colspan="2">Small: S</td></tr>
<tr><td colspan="6">Characteristics of the fibre :</td></tr>
<tr><td colspan="3">Flatness: f = S / I</td><td colspan="3">Elongation: e = I / L</td></tr>
<tr><td colspan="6">Density ratio:</td></tr>
<tr><td colspan="6">$\rho' = \rho_p / \rho$</td></tr>
<tr><td colspan="6">Form factor:</td></tr>
<tr><td colspan="3">Stokes: $F_S = f\ e^{1.3}$</td><td colspan="3">Newton: $F_N = f^2\ e$</td></tr>
<tr><td colspan="6">Drag corrections:</td></tr>
<tr><td colspan="2">Random Orientation:</td><td colspan="2">Horizontal orientation:</td><td colspan="2">Average Orientation:</td></tr>
<tr><td>Stokes:</td><td>Newton:</td><td>Stokes:</td><td>Newton:</td><td>Stokes:</td><td>Newton:</td></tr>
<tr><td>$k_{S,rand} = \frac{\left(F_S^{1/3} + F_S^{-1/3}\right)}{2}$</td><td>$k_{N,rand} = 10^{\alpha(-log(F_N))^{\beta}}$</td><td rowspan="2">$k_{S,hor} = \frac{\left(F_S^{0.05} + F_S^{-0.36}\right)}{2}$</td><td rowspan="2">$k_{N,hor} = 10^{0.77(-log(F_N))^{0.63}}$</td><td rowspan="2">$k_{S,A} = \frac{k_{S,rand} + k_{S,hor}}{2}$</td><td rowspan="2">$k_{N,A} = \frac{k_{N,rand} + k_{N,hor}}{2}$</td></tr>
<tr><td colspan="2">$\alpha = 0.45 + \frac{10}{exp\left(2.5\ log(\rho')\right)} + 30$
$\beta = 1.0 - \frac{37}{exp\left(3\ log(\rho')\right)} + 100$</td></tr>
<tr><td colspan="6">Drag Coefficient for Fibers:</td></tr>
<tr><td colspan="6">$C_D = \frac{24k_{S,A}}{R_e}\left(1 + 0.125\left(R_e k_{N,A}/k_{S,A}\right)^{2/3}\right) + \left(\frac{0.46k_{N,A}}{1 + \frac{5330}{\left(R_e k_{N,A}/k_{S,A}\right)}}\right)$</td></tr>
</table>

Dry settling of MNP aggregates

The atmospheric behaviour of MNP aggregates is influenced by their fractal dimension and structure, porosity, and permeability, which are defined below.

Fractal dimension of aerosol:

Depending on which media the aggregation occurred, aggregates may have different fractal dimensions. Particles and aggregates formed in water may be released to the atmosphere through aerosolisation through various mechanisms such as splashing, evaporation, or the creation of fine droplets, which are then suspended in the air. If the aggregation process occurs in freshwater and a significant potential barrier exists between particles, the aggregation is a Reaction Limited Aggregation (RLA) process (Sposito 1994). Simulation modelling and experimental investigations of RLA produce aggregates with df ~ 2.1 [19–22]. If no significant potential barrier exists between particles or if the aggregation occurs in the ocean (then screening the potential barriers between particles due to ionic strength), the formation of the aggregate is Diffusion Limited Aggregation (DLA), During DLA, aggregates of particles collide and combine, without optimising packing density into a close-fitting, organised structure. The resulting aggregate is porous and convoluted. The theoretical value of df for aggregates formed in the DLA regime water in three dimensions is ~1.8 [19]. If the aggregates were formed in the atmosphere, different fractal dimensions were reported from 1.35 to 1.89 (as in the DLA regime), with a mean fractal dimension of 1.65 ± 0.15 from urban aerosols[23,24].

Porosity:

Increased porosity within aggregates will result in a lower bulk density compared to individual particles of the same size. The impact of aggregate porosity on settling can be addressed by the inclusion of a porosity term (Po) in the settling equations (to represent the effective density difference of the aggregate). For the Stokes equation this results in:

$$v_s = \frac{v_g C_c}{\chi}(1 - \mathrm{Po}) \qquad \text{Eq. S8}$$

The relationship between the porosity Po of an aggregate with volume V_A, and number of monodisperse particles N in the aggregate, each with volume V_0, is:[25]

$$(1 - \mathrm{Po}) = \frac{NV_0}{V_A} \qquad \text{Eq. S9}$$

For N polydisperse primary particles of different volumes V_i in the aggregate, this becomes:

$$(1 - \mathrm{Po}) = \frac{\sum_{i=1}^{N} V_i}{V_A} \qquad \text{Eq. S10}$$

$$v_s = \frac{v_g C_c}{\chi}\left(\frac{\sum_{i=1}^{N} V_i}{V_A}\right) \quad \text{Eq. S11}$$

The porosity Po of an aggregate is also related to its size and the fractal dimension of the aggregate [25,26]:

$$(1 - \mathrm{Po}) = k_x \left(\frac{R_x}{r_p}\right)^{d_f - 3} \quad \text{Eq. S12}$$

With r_p as the radius of the primary particles, d_f the fractal dimension of the aggregate, R is the radius of the aggregate, the subscript x refers to a particular way of defining the radius R of the aggregate (hydrodynamical radius, radius of gyration), and k is the structure prefactor consistent with x definition, (also referred to as lacunarity or structure factor).

$$k_x = \frac{N}{\left(\frac{R_x}{r_p}\right)^{d_f}} \quad \text{Eq. S13}$$

For polydisperse primary particles in the aggregate, r_p can be substituted by size distribution [26]:

$$r_p = \left(\frac{\sum_{i=1}^{N} N_i r_i^3}{\sum_{i=1}^{N} N_i r_i^{d_f}}\right)^{1/(3-d_f)} \quad \text{Eq. S14}$$

Eq. S8 or Eq. S11 will be preferred depending on specific available data.

Permeability:

Macropores formed between particle clusters in aggregates can permit internal air flow [27]. This permeability affects the settling velocity by decreasing aggregate drag and increasing settling velocity compared to an impermeable particle of the same size and density.[26,28] Previous observations indicate that the settling velocities of large permeable aggregates could be at least twice as fast as impermeable particles of the same size and density.[25,29–31]

The settling velocity of a permeable aggregate v_p is related to the impermeable settling velocity v_g by [32,33]:

$$\Gamma = \frac{v_p}{v_g} = \frac{\zeta}{\zeta - \tanh\zeta} + \frac{3}{2\zeta^2} \quad \text{Eq. S15}$$

With ζ the dimensionless permeability of the porous aggregate is defined as, based on the Brinkman equation for non-uniform permeability [34] :

$$\zeta = \frac{r_c}{\sqrt{\kappa_p}} \qquad \text{Eq. S16}$$

And κ_p the floc permeability defined as:

$$\kappa_p = \frac{d_p^2}{72} \times \left(3 + \frac{4}{(1 - Po)} - 3\sqrt{\frac{8}{(1 - Po)} - 3} \right) \qquad \text{Eq. S17}$$

With r_c the size of larger clusters forming the aggregate (cluster-fractal model, introducing the non-uniformity of permeability).

To gain a comprehensive understanding of the primary factors influencing the dry settling and deposition of aggregates, we conducted calculations based on two scenarios: one that considers only the size and density of a non porous, non permeable particles (referred to as 'Compact'), and the second factoring in size, density, porosity, and permeability ('Permeable'). To the best of our knowledge, there is currently no experimental data available for MNPs. To accurately represent airborne aggregates, we derived key parameters from the fractal analysis studies conducted by Katrinak et al.[23] on carbonaceous aggregates from aerosols. The results are presented in Table Table S5 and

Figure ***S4***.

Table S5: Based on experimental data from aggregate aerosols from Katrinak et al.,[23] we calculate the porosity P and permeability factors (equations in supplementary information in the section aggregates)

Fractal Dimension d_f	**Aggregates diameter d_{agg} (mm)**	**Particle diameter d_p (nm)**	**Number of particles in the aggregate N**	**Calculated porosity Po**	**Calculated permeability factor Γ**
1.43	1.74	25	1341	99.82%	1.10
1.73	2.04	25	1403	99.52%	1.04
1.83	2.61	30	1335	99.31%	1.03

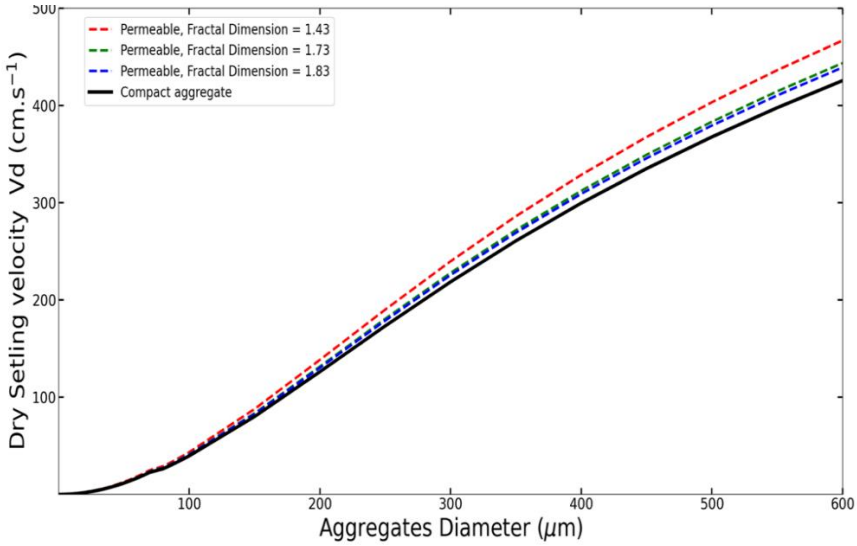

Figure S4: Impact of the fractal dimension, and induced permeability of MNP aggregate on the dry settling velocity on the example of PVC aggregates of varying diameter.

Section S2.2: Resistance to dry deposition

Impact of land surface characteristics on dry deposition

A pioneering approach to describe the influence of land surface characteristics on dry deposition was proposed by Slinn in 1982[35] for vegetative canopies and subsequently developed by Peters and Eiden (1992)[36] for a spruce forest and by Giorgi (1986)[37] for four surface types: smooth; with bluff roughness elements; oceans and vegetative canopies. These models appear to work well for larger particles but predict much lower deposition velocities for sub-micron aerosols compared to recent observations. Zhang et al. (2001),[38] therefore, modified the approach to include 15 *land use categories* (*LUCs*) and 5 seasonal categories (Table S5) resulting in a better description of sub-micron particle behaviour. This model has become a reference for particle dry deposition, including incorporation in large-scale models[39–44]. The model includes the aerodynamic resistance R_a, surface resistance R_s (Brownian, interception, and impaction collection efficiencies of particles by different surfaces) and rebound of particles on dry surfaces (Equations detailed hereafter).

Table S6: Land use categories (LUC) and seasonal categories (SC) based on the framework proposed by Zhang et al. [38] for the surface resistance.

Land use categories (LUC)	Definition
1	Evergreen needleleaf trees
2	Evergreen broadleaf trees
3	Deciduous needleleaf trees
4	Deciduous broadleaf trees
5	Mixed broadleaf and needleleaf trees
6	Grass
7	Crops, mixed farming
8	Desert
9	Tundra
10	Shrubs and interrupted woodlands
11	Wet land with plants
12	Ice cap and glacier
13	Inland water
14	Ocean
15	Urban
Seasonal categories (SC)	**Definition**
1	Midsummer with lush vegetation
2	Autumn with cropland that has not been harvested
3	Late autumn after frost, no snow
4	Winter, snow on ground and subfreezing
5	Transitional spring with partially green short annuals

The aerodynamic resistance, R_A: available for vertical maximum extent from the surface of 100 m[45] , the aerodynamic resistance depends on the height of the canopy z_R (m), the roughness length from the land z_o (m), ψ_H is the stability function (-), κ is the von Karman constant (-), and u_* is the friction velocity (m.s^{-1}).

$$R_A = \frac{ln\left(\frac{z_R}{z_0}\right) \mp \psi_H}{\kappa u_*} \qquad \text{Eq. S18}$$

For all type of surfaces, the stability function $\psi_H$is defined as, depending on the stability of the atmosphere, based on the Monin-Obukhov length (cf, **Error! Reference source not found.**):

$$\psi_H = \begin{cases} 1 + 4{,}7(\tau_r - \tau_0)\,, & \text{(stable)} \\ 0\,, & \text{(neutral)} \\ \ln\left(\dfrac{(\delta_0^2+1)(\delta_0+1)^2}{(\delta_r^2+1)(\delta_r+1)^2}\right) + 2\left(tan^{-1}(\delta_r) - tan^{-1}(\delta_0)\right), & \text{(unstable)} \end{cases} \qquad \text{Eq. S19}$$

Where L_{MO} is the Monin–Obukhov length, $\tau_0 = z_0/L_{MO}$, $\tau_r = \frac{z_r}{L_{MO}}$, $\delta_0 = (1-15\tau_0)^{1/4}$, and $\delta_r = (1-15\tau_r)^{1/4}$

The relation between the friction velocity $u_*$and the surface wind velocity at the height z, $u_{(z)}$, (often more available experimentally for z equal to 5 meters, called in the paper u_s) is given by[46,47]:

$$u_* = \frac{\kappa u_{(z)}}{ln\left(\frac{z}{z_0}\right)} \qquad \text{Eq. S20}$$

If the roughness length of land surfaces is fixed, the roughness length for water surfaces changes with the wind speed. The impact of the wind on roughness length of the water surface is accounted for under neutral conditions, mean winds [48–50]:

$$z_0 = \frac{0.11\nu_A}{u_*} + \frac{0.011u_*^2}{g} \qquad \text{Eq. S21}$$

For other meteorological cases, as high winds in tropical cyclones as example, specific description of z0 need to be done (cf. Powell et al. [47] for specific methodology).

The surface resistance, R_S or quasilaminar resistance : depends on the collection efficiency of the surface:

$$R_S = \frac{1}{\varepsilon_0 u_*\left(E_{Br} + E_{In} + E_{Imp}\right)R_i} \qquad \text{Eq. S22}$$

With ε_0 an empirical constant that was taken to equal a value of 3 for all land use types by Zhang et al.[38], u_* the friction velocity ($m.s^{-1}$).

R_i represents the fraction of particles stuck to a surface. Particles larger than 5 mm may rebound after hitting a surface. This process may be included by modifying the total collection efficiency by the factor of R_i, which represents the fraction of particles sticking to the surfaces. For wet surfaces, there is no rebound, else:

$$R_i = exp\left(-St^{1/2}\right) \qquad \text{Eq. S23}$$

With St the Stokes number, $St=v_g u_*/gA$ for vegetated surfaces (Slinn, 1982), A is the characteristic radius of collectors. For smooth surfaces or with bluff roughness surfaces, $St=v_g u_*^2/n$ (Giorgi, 1988).

E_{Br}, E_{In} and E_{Imp} are the collection efficiencies of Brownian diffusion, interception, and impaction, respectively, defined as:

For the collection efficiencies of Brownian diffusion E_{Br}:

$$E_{Br} = Sc^{-\gamma} \quad \text{Eq. S24}$$

With Sc is the Schmidt number, given as the ratio of the kinematic viscosity of air, ν_A, to the particle Brownian diffusivity, D_{diff_Br}: $Sc=\nu_A/D_{diff\_Br}$. γ usually lies between 1/2 for smooth surfaces, as surface water, to 2/3 for rougher surfaces as vegetated surfaces.

For the collection efficiencies of interception E_{In}:

$$E_{In} = 0.5\left(\frac{d_p}{A}\right)^2 \quad \text{Eq. S25}$$

The characteristic radius A is given for different land use and seasonal categories [38].

For the collection efficiencies of impaction E_{Imp}:

$$E_{Imp} = \left(\frac{St}{\alpha + St}\right)^{\beta} \quad \text{Eq. S26}$$

With α and β are constants. With α =0.8 and β =2 best fit is obtained for the data collected by Belot and Gauthier[51], based on Peters and Eiden[36].

Here, the Stokes number St is defined as:

- For smooth surfaces or surfaces with bluffs roughness elements:

$$St = \frac{v_s u_*^2}{g\nu_A} \quad \text{Eq. S27}$$

- For vegetated surfaces:

$$St = \frac{v_s u_*}{gA} \quad \text{Eq. S28}$$

Figure S5 highlights the impact of the aerodynamic resistance, and surface resistance variation depending on the size of the particle, for a specific LUC: With all elements considered (v_g, R_a, R_s and rebounds), we can see that the dry deposition does not arise from the same mechanism regardless of particle size. In this model, rebounds cannot be neglected for particles with sizes of 1 μm or larger, as they are influenced by interception, impaction, and gravitational regimes. The gravitational settling becomes the main mechanism on the dry deposition velocity for particles of diameter higher than 200 μm.

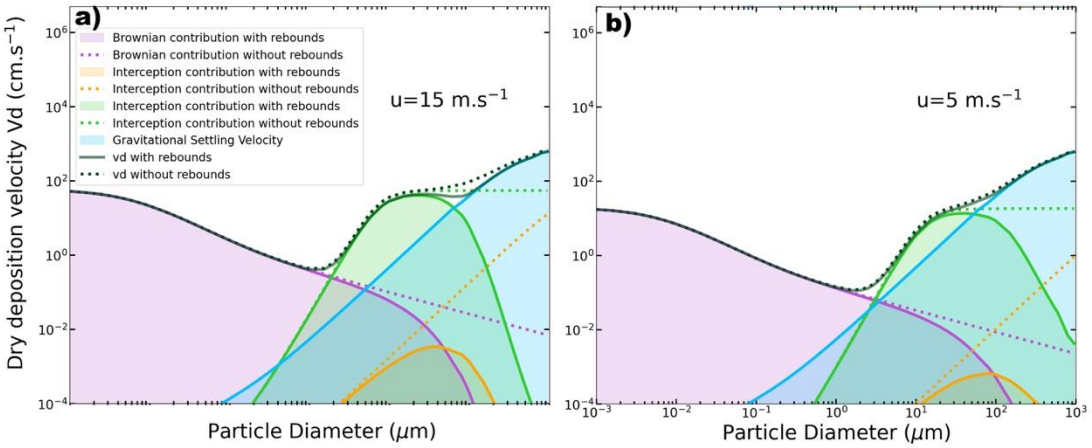

Figure S5: Contributions of Brownian motion, interception, and impaction on collection efficiencies of PVC MNP on evergreen broadleaf tree surfaces. These contributions are calculated with different MNPs diameters for two wind speeds (a) u = 15 m s-1, and b) u = 5 m s-1, bottom), in neutral stratification, in midsummer season with lush vegetation. The impact of particle rebound is also shown separately via the dotted lines. Higher surface wind speeds lead to a higher predicted dry deposition velocity with more impact of rebounds.

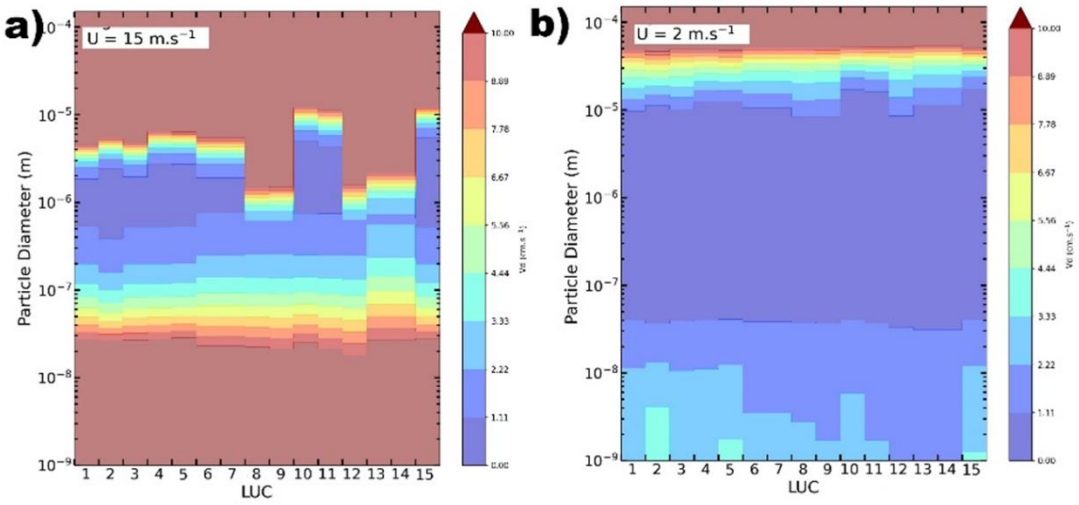

Figure S6: Impact of Particle Diameter, Wind Speed, and Land-Use Categories on the Dry Deposition Velocity of High-Density PE Particles: a) Variation of the dry deposition velocity as a function of HD-PE diameter and LUCs with surface wind U=15 m.s^{-1}, season: midsummer with lush vegetation, neutral stratification, with LUCs numbering presented in legend **b)** Variation of the dry deposition velocity as a function of HD-PE diameter and LUCs with surface wind U=2 m.s^{-1}, season: midsummer with lush vegetation, neutral stratification.

Atmospheric stratification:

In dry deposition of MNPs, the atmospheric stratification needs to be considered, specifically for small MNPs lower than 1micrometer for all surface winds, or 10^2 micrometer for hight surface winds (cf. Figure 4 of the present article). This stratification depends on the surface temperature and the temperature of the air above. The Monin-Obukhov Length classification[52] is used to classify atmospheric stability. This classification is presented in Figure S7 a).The small particles are more affected by the stratifications of the atmosphere due to their size and the vs mixing of the atmosphere as the result of difference in temperatures (as schematized in Figure S7 b)

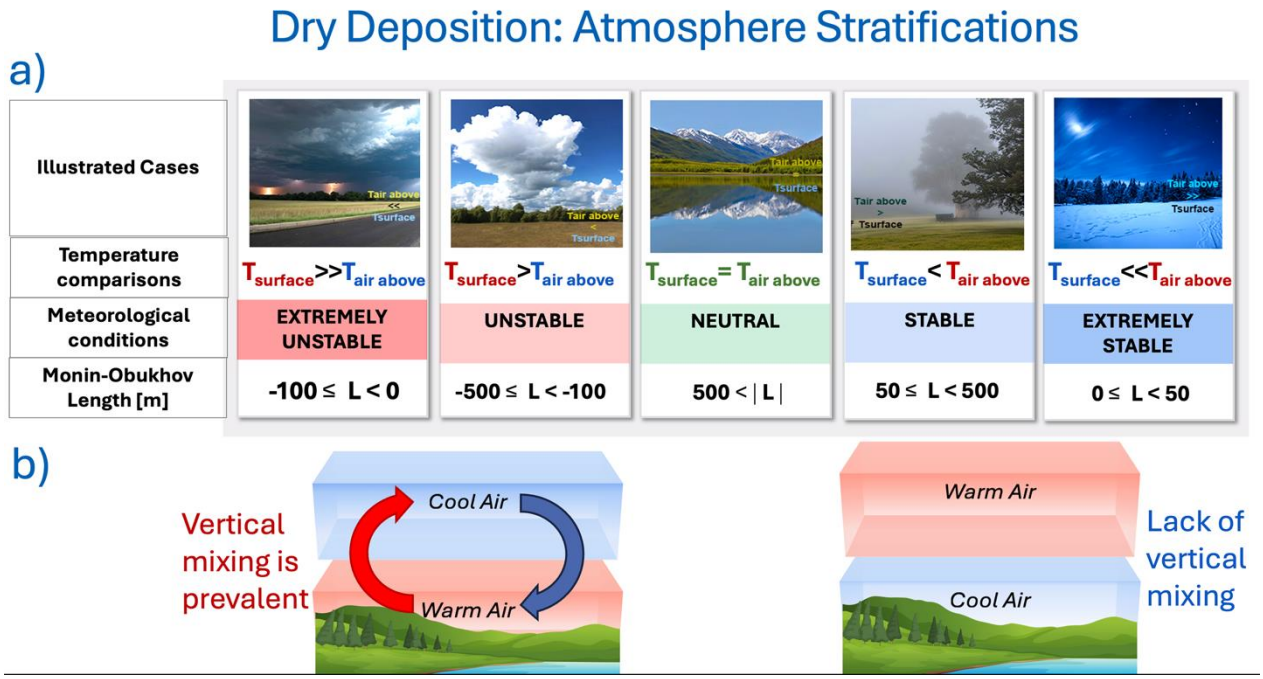

Figure S7: Atmosphere stratifications effects on the dry deposition a) Monin-Obukhov length classification for atmospheric stability[52], b) Two schematic diagrams illustrating the concept of atmospheric stratification (illustration created with latent diffusion model[53] and modified with Adobe Photoshop)

Section S3: Wet deposition

Section S3.1: Below-cloud scavenging

The time-dependent removal of MNPs by below-cloud scavenging (BCS) can be described as a first-order decay process:[54]

$$\left.\frac{dC}{dt}\right|_{BCS} = -\lambda_p C \qquad \text{Eq. S29}$$

where C is the atmospheric concentration of MNPs (μg m^{-3}) and λ_p is the scavenging coefficient (in s^{-1})
The scavenging coefficient can be calculate as (see developments in [45]):

$$\lambda_p = \int_0^\infty \frac{\pi}{4}\left(D_p + d_p\right)^2 \left(V\left(D_p\right) + v\left(d_p\right)\right) E\left(d_p, D_p\right) N(D_p) dD_p \qquad \text{Eq. S30}$$

where D_p and d_p are the raindrop and MNP diameter respectively (m), $V(D_p)$ and $v(d_p)$ the raindrop and the particle terminal velocities, respectively, $E(d_p, D_p)$ is the collision efficiency of an MNP with a raindrop, and $N(Dp)$ the raindrop size distribution

For a monodispersed representative droplet diameter Dp, Eq. S30 becomes:[55]

$$\lambda_p = \frac{3}{2} Eeff \frac{RI}{(Dp/2)} \qquad \text{Eq. S31}$$

where RI the rainfall intensity (mm s^{-1}). Eeff is the collection efficiency.

The classical Slinn model[56] was the first approach to calculate the dominant size-dependent processes governing E for BCS which include scavenging due to Brownian diffusion, interception and inertial impaction of particles by raindrops. The following secondary processes have since been added to correct for the underprediction in collision efficiency: thermophoresis, diffusiophoresis and electrophoresis.

Calculated values of λ_p should integrate the full range of collection efficiencies (from low for larger raindrops to high for smaller raindrops: Loosmore and Cederwall[57] 2004) over the range of raindrop diameters in any given storm. Despite the sensitivity of λ_p to the raindrop size distribution [55] a uniform raindrop size is a reasonable simplification if an appropriate representative diameter is chosen (e.g. the median diameter for a gamma raindrop size distribution: [57,58].

$$D_P = 1.94\, RI^{0.158} \qquad \text{Eq. S32}$$

with Dp expressed in mm and RI in mm h^{-1}. In the present work, tested four different RI categories: (1) drizzle with RI < 0.5 mm h^{-1}, (2) moderate rain with 0.5 mm h^{-1} < RI < 4 mm h^{-1}, (3) heavy rain with 4 mm h^{-1} < RI < 8 mm h^{-1}, (4) very heavy rain with RI > 8 mm h^{-1}.

Collision efficiency:

a) Brownian diffusion

Collision efficiency with Brownian diffusion for ultra-fine particles (≤ 0.1 mm), that move unpredictably against the air flow around the raindrop:

$$E_{Br}(d_p, D_p) = \frac{4}{Re_r Sc}\left[1 + 0.4{Re_r}^{1/2}Sc^{1/3} + 0.16{Re_r}^{1/2}Sc^{1/2}\right] \quad \text{Eq. S33}$$

Where Re_r the raindrop Reynolds number:

$$Re_r = \frac{\rho v_g d_p}{\mu} \quad \text{Eq. S34}$$

Where Sc the particle Schmidt number:

$$Sc = \frac{\mu_a}{\rho_g D_{diff\_Br}} \quad \text{Eq. S35}$$

The particle Brownian diffusivity coefficient :

$$D_{diff\_Br} = \frac{k_B T_a C_c}{3\pi\mu_a \mathrm{d}_p} \quad \text{Eq. S36}$$

The Cunningham correction factor :

$$C_c = 1 + \frac{2\lambda}{\mathrm{d}_p}\left(1.257 + 0.4exp\left(-0.55\frac{d_p}{\lambda}\right)\right) \quad \text{Eq. S37}$$

With λ the mean free path of air molecules ,μ_a the air viscosity , ρ_a the air density, T_a the air temperature (K), d_p the particle diameter , D_p the rain drop diameter , k_B the Boltzmann constant , $V(\mathrm{D_p})$the raindrop terminal velocity

b) Interception

Interception occurs when coarse particles are directly within a collection area of the falling raindrop and is thus independent of the particle's mass or inertia:

$$E_{In}(D_p, d_p) = 4\frac{d_p}{D_p}\left[\frac{\mu_a}{\mu_w} + \frac{d_p}{D_p}\left(1 + 2{Re_r}^{1/2}\right)\right] \quad \text{Eq. S38}$$

386

387 **c) Impaction**

388 Inertial impaction collects coarse particles with large masses that are unable to move with the streamlines
389 around the falling raindrop:

$$E_{Imp}(, d_p, D_p) = \left(\frac{St - St^*}{St - St^* + 2/3}\right)^{3/2} \quad \text{Eq. S39}$$

390

391 Where:

$$St = \frac{2\tau\left(V(D_p) - v(d_p)\right)}{D_p} \quad \text{Eq. S40}$$

392

$$\tau = \frac{(\rho_p - \rho_a)d_p^2 C_c}{18\mu_a} \quad \text{Eq. S41}$$

393

$$St^* = \frac{1.2 + \frac{1}{12}ln(1 + Re_r)}{1 + ln(1 + Re_r)} \quad \text{Eq. S42}$$

394

395 **d) Thermophoresis**

396 Thermophoresis, which is caused by uneven heating of particles in ambient temperature gradients, drives
397 particles towards evaporating and sublimating hydrometeors. Thermophoresis efficiency term needs the
398 thermal conductivity k_p of the particles as parameter.

399

$$E_{th}(d_p, D_p,) = \frac{4\alpha_{th}\left(2 + 0.6{Re_r}^{1/2}{P_r}^{1/3}\right)(T_a - T_S)}{V(D_p)D_p} \quad \text{Eq. S43}$$

400

401 Where

$$\alpha_{th} = \frac{2C_c(k_a + 5\lambda/D_p k_p)k_a}{5P(1 + 6\lambda/D_p)(2k_a + k_p + 10\lambda/D_p k_p)} \quad \text{Eq. S44}$$

402

$$P_r = \frac{C_p \mu_a}{k_a} \qquad \text{Eq. S45}$$

403 k_a and k_p are the thermal conductivity of the air and the particle, respectively, T_a and T_S the temperature of
404 air and the raindrop surface, Cp the specific heat capacity of air, P the atmospheric pressure
405 For amorphous polymers, this constant is low (< 0.5 W/m K at T=25 °C on the different examples):[59]
406

407 *Table S7: Thermal conductivities and densities of some polymers, data from [59–61]*

Material	Thermal Conductivity 25°C ($W \cdot m^{-1} \cdot K^{-1}$)	Density ($kg.m^{-3}$)
Low-Density Polyethylene (LD-PE)	0.30	920
High-Density Polyethylene (HD-PE)	0.44	980
Polypropylene (PP)	0.11	910
Polystyrene (PS)	0.14	1071
Poly methylmethacrylate (PMMA)	0.21	1187
Nylon-6 (PA)	0.25	1130
Nylon-6,6 (PA66)	0.26	1166
Polyethylene terephthalate (PET)	0.15	1380
Poly butylene terephthalate (PBT)	0.29	1300
Polycarbonate (PC)	0.20	1200
Poly acrylonitrile-butadiene-styrene copolymer (ABS)	0.33	1100
Poly etheretherekitone (PEEK)	0.25	1260
Polyethylene sulfite (PPS)	0.30	1350
Polysulfone (PSU)	0.22	1250
Polyphenylsulfone (PPSU)	0.35	1300
Polyvinyle chloride (PVC)	0.19	1580
Polyvinylidene difluoride (PVDF)	0.19	1800
Polytetrafluoroethylene (PTFE)	0.27	2200
Polyethylene vinyl acetate (EVA)	0.34	930
Polyimide, thermoplastic (PI)	0.11	1300

408

e) Diffusiophoresis

Diffusiophoresis moves particles towards diffusional-growing hydrometeors due to water vapour concentration gradients:[62]

$$E_{dph}(D_p, d_p) = \frac{4\beta_{dph}\left(2 + 0.6Re_r^{1/2}Sc_w^{1/3}\right)\left(\frac{P_s^0}{T_s} - \frac{P_a^0 RH}{T_a}\right)}{V(D_p)D_p} \quad \text{Eq. S46}$$

Where

$$\beta_{th} = \frac{T_a D_{diff\_Water}}{P}\sqrt{\frac{M_w}{M_a}} \quad \text{Eq. S47}$$

$$Sc_w = \frac{\mu_a}{\rho_a D_{diffWater}} \quad \text{Eq. S48}$$

D_{diff_Water} : water vapour diffusivity in air ($m^2.s^{-1}$), RH relative humidity (%),

f) Electrophoresis

Electrophoresis (electric charge effect) occurs when raindrop with a charge Q_r attracts a particle with an opposite charge q_p. This process enhances the capture efficiency.[63]

$$E_{ec}(D_p, d_p) = \frac{16KC_c Q_r q_p}{3\pi\mu_a V(D_p)D_p^2 d_p} \quad \text{Eq. S49}$$

where K =9×109 (in $N.m^2.C^{-2}$), Q_r and q_p are the mean charges on the raindrop and on the aerosol particle (in Coulomb, C) assumed to be of opposite sign. A parameterization, with respect to size, has been proposed for the mean raindrop and particle charges:

$$Q_r = a\alpha D_p^2 \quad \text{Eq. S50}$$

$$q_p = a\alpha d_p^2 \quad \text{Eq. S51}$$

Here, a=0.83×10−6 and α (C m−2), an empirical parameter, spans the range from 0, indicating neutral particles, to 7, indicative of highly electrified clouds linked with thunderstorms. [63,64]

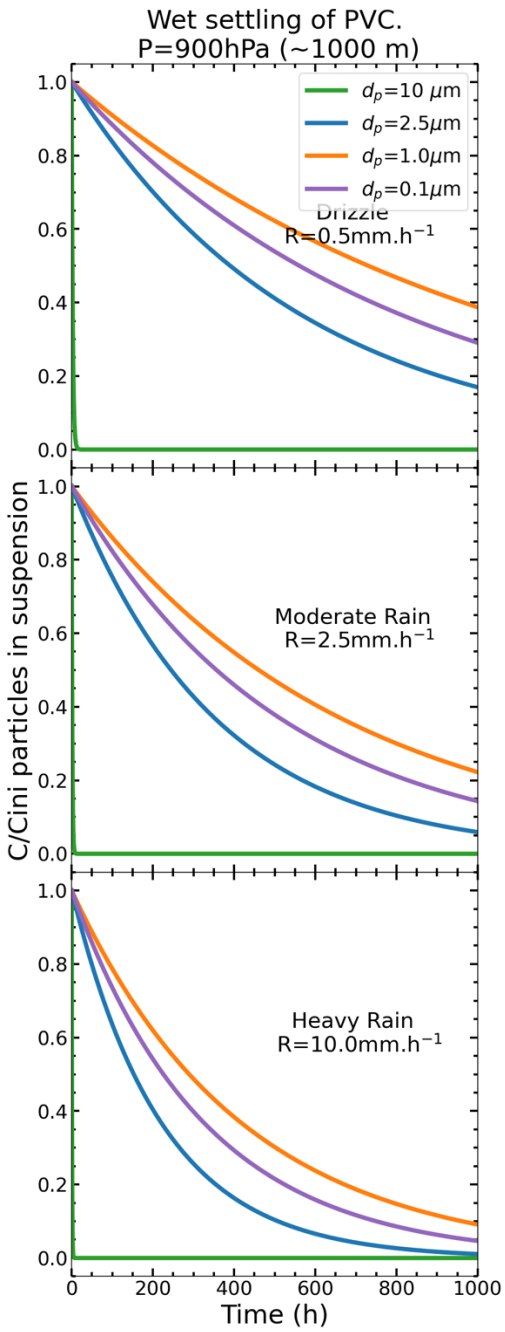

Figure S8: Wet settling half lives of PVC

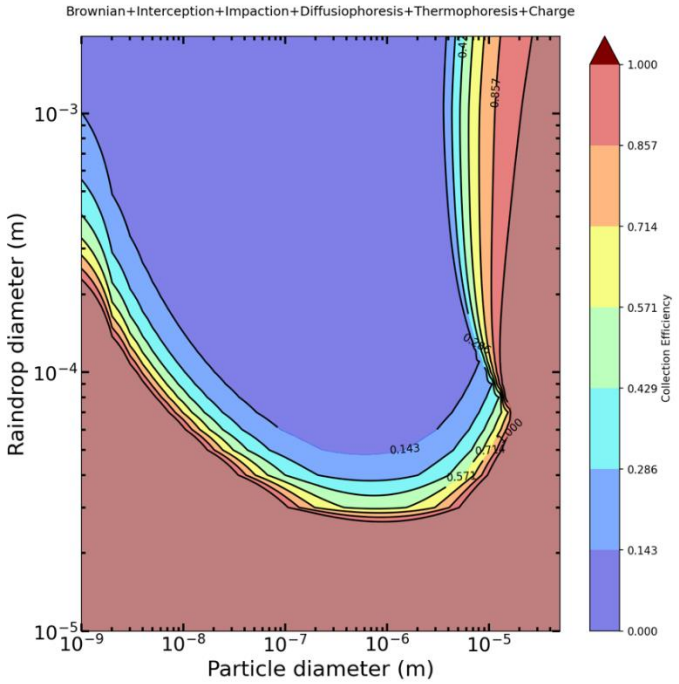

Figure S9: The efficiency probability of scavenging a particle as function of its size and the raindrop size

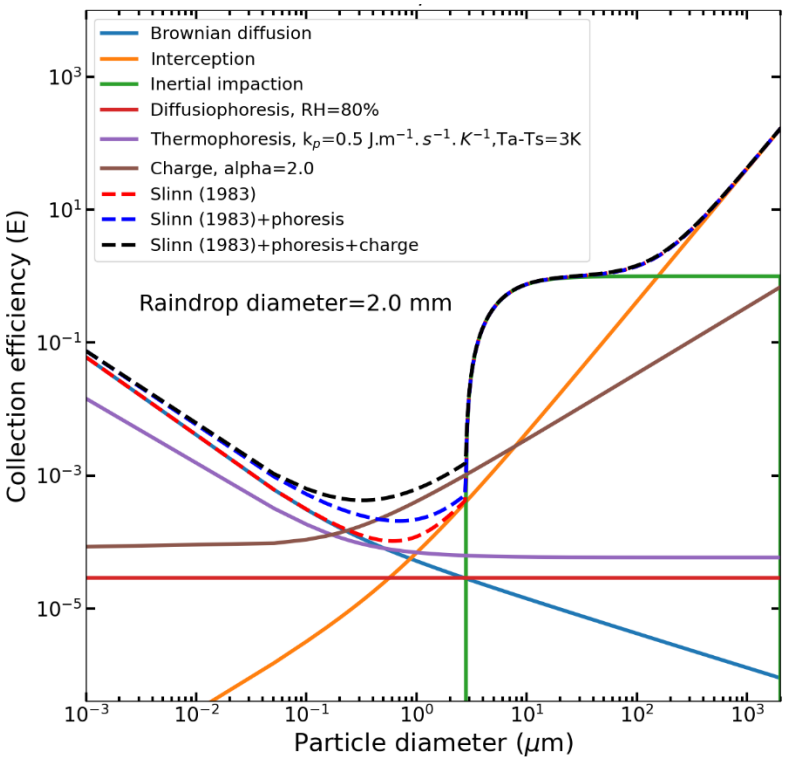

Figure S10: Variation of MNPs total and detailed collection efficiencies with a raindrop diameter of 2 mm. Contribution to the collection efficiency with T=283.65K, P=850hPa. The importance of considering phoresis and charge is emphasized for particles of diameters of around 1 µm.

Section S3.2: In-cloud scavenging

Photoaging

Table S8: Photoaging impact on the wettability of seven plastics, data from Huang et Wang.[65] A contact angle between 90° and 180° is classified as having a low wettability. A contact angles between 0º and 90º correspond to a high wettability (in bold), and a contact angle of 0º a perfect wetting.

Plastics		**Contact Angle θ Before Photoaging**	**Contact Angle θ After Photoaging**
PVC	Polyvinyl chloride	93.40º	92.10 º
ABS	Acrylonitrile butadiene styrene plastic	96.50 º	94.54 º
PMMA	Polymethyl methacrylate	**88.38 º**	**83.87 º**
PC	Polycarbonate	91.64 º	**81.71 º**
PET	Polyethylene glycol terephthalate	98.40 º	**69.50 º**
PE	Polyethylene	100.51 º	**64.30 º**
PS	Polystyrene	98.70 º	**57.90 º**

As shown in Figure S1, in the MNPs length scales (from 1μm to 5 mm), no insoluble particles with a wetting contact angle higher than 12º can condense water at their surface in the typical range of supersaturation S in natural clouds (between 1.0 and 1.01, with a probable absolute maximum value of S in natural clouds of 1.03 (RH=103%)). For the studied plastics by Huang et Wang in Table S9, by applying Eq. 9 of the main article, the photoaging process alone does not allows these MNPs to become a CCN.

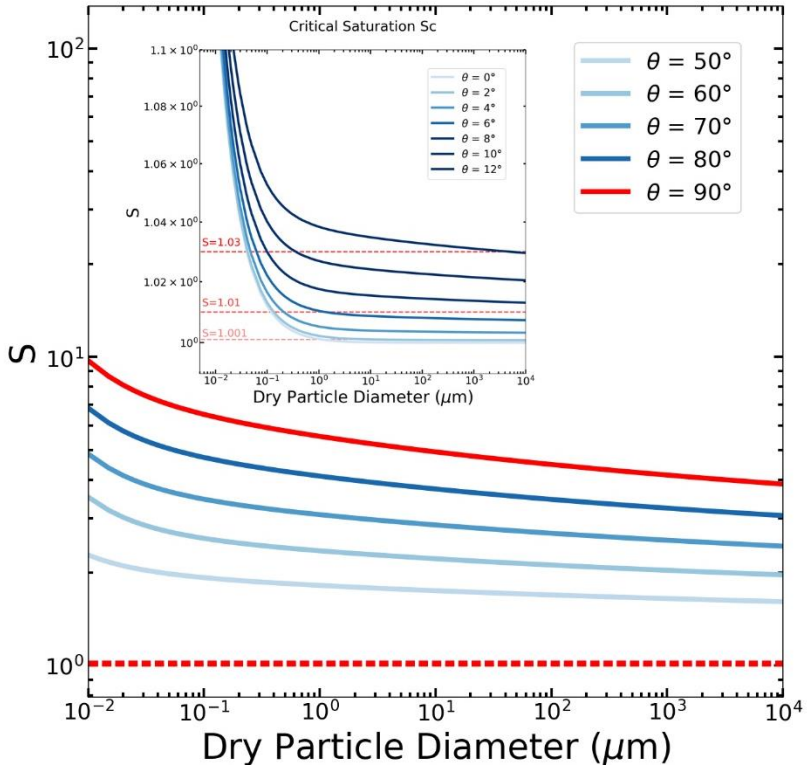

Figure S11. Variation of Critical Saturation (Sc) curves for spherical insoluble particles is presented as a function of particle diameter and contact angle (wettability). These curves are calculated using Eq. 9 at a temperature of 0°C. The figure illustrates that at the maximum supersaturation (S=1.03, represented by the red dashed line) typically found in Earth's atmosphere, none of the photoaging plastics in pure forms (with no aggregates, exterior molecules on the surface) can act as condensation nuclei for water. In the inset, contact angles (wettability) leading to the formation of water condensation nuclei are depicted for a supersaturation of 1.001, 1.01, and 1.03 (to facilitate the comparison with McDonald 1964[66]).

References

1. Farmer, D. K., Boedicker, E. K. & DeBolt, H. M. Dry Deposition of Atmospheric Aerosols: Approaches, Observations, and Mechanisms. *Annual Review of Physical Chemistry* **72**, 375–397 (2021).
2. Ghanem, A., Young, J. & Edwards, F. Settling velocity models applied to ballasted flocs - a review. *Saber* **25**, 247–253 (2013).
3. Fan, M., Su, D. & Yang, L. Development of a benchmark for drag correlations of nonspherical particles based on settling experiments of super-ellipsoidal particles. *Powder Technology* **409**, 117811 (2022).
4. Kalman, H. & Matana, E. Terminal velocity and drag coefficient for spherical particles. *Powder Technology* **396**, 181–190 (2022).
5. Jennings, S. G. The mean free path in air. *Journal of Aerosol Science* **19**, 159–166 (1988).
6. Cunningham, E. On the velocity of steady fall of spherical particles through fluid medium. *Proceedings of the Royal Society of London. Series A, Containing Papers of a Mathematical and Physical Character* **83**, 357–365 (1910).
7. Jennings, S. G. The mean free path in air. *Journal of Aerosol Science* **19**, 159–166 (1988).
8. Kulkarni, P., Baron, P. A. & Willeke, K. *Aerosol Measurement: Principles, Techniques, and Applications*. (John Wiley & Sons, 2011).
9. Sundaram, S. K., Ohji, T., Fox, K. M. & Hoffman, E. *Advances in Materials Science for Environmental and Nuclear Technology II*. (John Wiley & Sons, 2011).
10. Wilson, L. & Huang, T. C. The influence of shape on the atmospheric settling velocity of volcanic ash particles. *Earth and Planetary Science Letters* **44**, 311–324 (1979).
11. Crowder, T. M., Rosati, J. A., Schroeter, J. D., Hickey, A. J. & Martonen, T. B. Fundamental Effects of Particle Morphology on Lung Delivery: Predictions of Stokes' Law and the Particular Relevance to Dry Powder Inhaler Formulation and Development. *Pharm Res* **19**, 239–245 (2002).
12. Hassan, M. S. & Lau, R. W. M. Effect of Particle Shape on Dry Particle Inhalation: Study of Flowability, Aerosolization, and Deposition Properties. *AAPS PharmSciTech* **10**, 1252 (2009).
13. Aeschlimann, M., Li, G., Kanji, Z. A. & Mitrano, D. M. Potential impacts of atmospheric microplastics and nanoplastics on cloud formation processes. *Nat. Geosci.* **15**, 967–975 (2022).
14. Bagheri, G. & Bonadonna, C. On the drag of freely falling non-spherical particles. *Powder Technology* **301**, 526–544 (2016).
15. Coyle, R., Service, M., Witte, U., Hardiman, G. & McKinley, J. Modeling Microplastic Transport in the Marine Environment: Testing Empirical Models of Particle Terminal Sinking Velocity for Irregularly Shaped Particles. *ACS EST Water* **3**, 984–995 (2023).
16. Saxby, J., Beckett, F., Cashman, K., Rust, A. & Tennant, E. The impact of particle shape on fall velocity: Implications for volcanic ash dispersion modelling. *Journal of Volcanology and Geothermal Research* **362**, 32–48 (2018).
17. Tatsii, D. *et al.* Shape Matters: Long-Range Transport of Microplastic Fibers in the Atmosphere. *Environ. Sci. Technol.* **58**, 671–682 (2024).
18. Chen, Q. *et al.* Long-range atmospheric transport of microplastics across the southern hemisphere. *Nat Commun* **14**, 7898 (2023).
19. Jullien, R., Botet, R. & Mors, P. M. Computer simulations of cluster–cluster aggregation. *Faraday Discuss. Chem. Soc.* **83**, 125–137 (1987).
20. Zhang, J. & Buffle, J. Multi-method determination of the fractal dimension of hematite aggregates. *Colloids and Surfaces A: Physicochemical and Engineering Aspects* **107**, 175–187 (1996).
21. Meakin, P. *Fractals, Scaling and Growth Far from Equilibrium*. (Cambridge University Press, 1998).
22. Seijo, M., Ulrich, S., Filella, M., Buffle, J. & Stoll, S. Modeling the Adsorption and Coagulation of Fulvic Acids on Colloids by Brownian Dynamics Simulations. *Environ. Sci. Technol.* **43**, 7265–7269 (2009).

23. Katrinak, K. A., Rez, P., Perkes, P. R. & Buseck, P. R. Fractal geometry of carbonaceous aggregates from an urban aerosol. *Environ. Sci. Technol.* **27**, 539–547 (1993).
24. Senesi, N. & Wilkinson, K. J. *Biophysical Chemistry of Fractal Structures and Processes in Environmental Systems*. (John Wiley & Sons, 2008).
25. Johnson, C. P., Li, X. & Logan, B. E. Settling Velocities of Fractal Aggregates. *Environ. Sci. Technol.* **30**, 1911–1918 (1996).
26. Bushell, G. C., Yan, Y. D., Woodfield, D., Raper, J. & Amal, R. On techniques for the measurement of the mass fractal dimension of aggregates. *Advances in Colloid and Interface Science* **95**, 1–50 (2002).
27. Li, X.-Y. & Logan, B. E. Permeability of Fractal Aggregates. *Water Research* **35**, 3373–3380 (2001).
28. Chellam, S. & Wiesner, M. R. Fluid mechanics and fractal aggregates. *Water Research* **27**, 1493–1496 (1993).
29. Hawley, N. Settling velocity distribution of natural aggregates. *Journal of Geophysical Research: Oceans* **87**, 9489–9498 (1982).
30. Li, D. & Ganczarczyk, J. Flow through activated sludge flocs. *Water Research* **22**, 789–792 (1988).
31. Li, X. & Logan, B. E. Collision Frequencies of Fractal Aggregates with Small Particles by Differential Sedimentation. *Environ. Sci. Technol.* **31**, 1229–1236 (1997).
32. Matsumoto, K. & Suganuma, A. Settling velocity of a permeable model floc. *Chemical Engineering Science* **32**, 445–447 (1977).
33. Li, X.-Y. & Logan, B. E. Permeability of Fractal Aggregates. *Water Research* **35**, 3373–3380 (2001).
34. Lee, D. J., Chen, G. W., Liao, Y. C. & Hsieh, C. C. On the free-settling test for estimating activated sludge floc density. *Water Research* **30**, 541–550 (1996).
35. Slinn, W. G. N. Predictions for particle deposition to vegetative canopies. *Atmospheric Environment (1967)* **16**, 1785–1794 (1982).
36. Peters, K. & Eiden, R. Modelling the dry deposition velocity of aerosol particles to a spruce forest. *Atmospheric Environment. Part A. General Topics* **26**, 2555–2564 (1992).
37. Giorgi, F. A particle dry-deposition parameterization scheme for use in tracer transport models. *Journal of Geophysical Research: Atmospheres* **91**, 9794–9806 (1986).
38. Zhang, L., Gong, S., Padro, J. & Barrie, L. A size-segregated particle dry deposition scheme for an atmospheric aerosol module. *Atmospheric Environment* **35**, 549–560 (2001).
39. Andersson, C., Langner, J. & Bergstroumm, R. Interannual variation and trends in air pollution over Europe due to climate variability during 1958–2001 simulated with a regional CTM coupled to the ERA40 reanalysis. *Tellus B: Chemical and Physical Meteorology* **59**, 77–98 (2007).
40. Ghan, S. J. & Easter, R. C. Impact of cloud-borne aerosol representation on aerosol direct and indirect effects. *Atmospheric Chemistry and Physics* **6**, 4163–4174 (2006).
41. Gong, W. *et al.* Cloud processing of gases and aerosols in a regional air quality model (AURAMS). *Atmospheric Research* **82**, 248–275 (2006).
42. Zakey, A. S., Solmon, F. & Giorgi, F. Implementation and testing of a desert dust module in a regional climate model. *Atmospheric Chemistry and Physics* **6**, 4687–4704 (2006).
43. Wang, Y. Q., Zhang, X. Y. & Arimoto, R. The contribution from distant dust sources to the atmospheric particulate matter loadings at XiAn, China during spring. *Science of The Total Environment* **368**, 875–883 (2006).
44. Heald, C. L. *et al.* Concentrations and sources of organic carbon aerosols in the free troposphere over North America. *Journal of Geophysical Research: Atmospheres* **111**, (2006).
45. Seinfeld, J. H. & Pandis, S. N. *Atmospheric Chemistry and Physics: From Air Pollution to Climate Change*. (John Wiley & Sons, 2016).
46. Panofsky, H. A. Determination of stress from wind and temperature measurements. *Quarterly Journal of the Royal Meteorological Society* **89**, 85–94 (1963).

47. Powell, M. D., Vickery, P. J. & Reinhold, T. A. Reduced drag coefficient for high wind speeds in tropical cyclones. *Nature* **422**, 279–283 (2003).
48. Charnock, H. Wind stress on a water surface. *Quarterly Journal of the Royal Meteorological Society* **81**, 639–640 (1955).
49. Smith, S. D. Coefficients for sea surface wind stress, heat flux, and wind profiles as a function of wind speed and temperature. *Journal of Geophysical Research: Oceans* **93**, 15467–15472 (1988).
50. Petroff, A. & Zhang, L. Development and validation of a size-resolved particle dry deposition scheme for application in aerosol transport models. *Geoscientific Model Development* **3**, 753–769 (2010).
51. Belot, Y. & Gauthier, D. *Transport of Micronic Particles from Atmosphere to Foliar Surfaces*. (1974).
52. Sathe, A., Mann, J., Barlas, T., Bierbooms, W. a. a. m. & van Bussel, G. j. w. Influence of atmospheric stability on wind turbine loads. *Wind Energy* **16**, 1013–1032 (2013).
53. Rombach, R., Blattmann, A., Lorenz, D., Esser, P. & Ommer, B. High-resolution image synthesis with latent diffusion models. in *Proceedings of the IEEE/CVF conference on computer vision and pattern recognition* 10684–10695 (2022).
54. Duhanyan, N. & Roustan, Y. Below-cloud scavenging by rain of atmospheric gases and particulates. *Atmospheric Environment* **45**, 7201–7217 (2011).
55. Wang, X., Zhang, L. & Moran, M. D. Uncertainty assessment of current size-resolved parameterizations for below-cloud particle scavenging by rain. *Atmospheric Chemistry and Physics* **10**, 5685–5705 (2010).
56. Slinn, W. G. N. Precipitation scavenging. *Atmospheric Science and Power Production* (1984).
57. Loosmore, G. A. & Cederwall, R. T. Precipitation scavenging of atmospheric aerosols for emergency response applications: testing an updated model with new real-time data. *Atmospheric Environment* **38**, 993–1003 (2004).
58. Willis, P. T. Functional Fits to Some Observed Drop Size Distributions and Parameterization of Rain. *Journal of the Atmospheric Sciences* **41**, 1648–1661 (1984).
59. Hashim, A. A. *Smart Nanoparticles Technology*. (BoD – Books on Demand, 2012).
60. Li, K., Xu, G., Huang, X., Xie, Z. & Gong, F. Manufacturing of Micro-Lens Array Using Contactless Micro-Embossing with an EDM-Mold. *Applied Sciences* **9**, 85 (2019).
61. Doğan, B. & Tan, H. The Numerical and Experimental Investigation of the Change of the Thermal Conductivity of Expanded Polystyrene at Different Temperatures and Densities. *International Journal of Polymer Science* **2019**, 1–9 (2019).
62. Chate, D. M. Study of scavenging of submicron-sized aerosol particles by thunderstorm rain events. *Atmospheric Environment* **39**, 6608–6619 (2005).
63. Andronache, C. Diffusion and electric charge contributions to below-cloud wet removal of atmospheric ultra-fine aerosol particles. *Journal of Aerosol Science* **35**, 1467–1482 (2004).
64. Andronache, C., Grönholm, T., Laakso, L., Phillips, V. & Venäläinen, A. Scavenging of ultrafine particles by rainfall at a boreal site: observations and model estimations. *Atmospheric Chemistry and Physics* **6**, 4739–4754 (2006).
65. Huang, Z. & Wang, H. Study on the impact of photoaging on the generation of very small microplastics (MPs) and nanoplastics (NPs) and the wettability of plastic surface. *Environ Sci Pollut Res* **30**, 92963–92982 (2023).
66. McDonald, J. E. Cloud nucleation on insoluble particles. *Journal of Atmospheric Sciences* **21**, 109–116 (1964).